

A direct demonstration of bulk-boundary correspondence in higher-order topological superconductors with chiral symmetry

Xiaoyu Zhu

School of Physics, MOE Key Laboratory for Non-equilibrium Synthesis and Modulation of Condensed Matter, Xi'an Jiaotong University, Xi'an, Shaanxi 710049, China

(Dated: March 27, 2024)

A higher-order topological superconductor can experience topological phase transitions driven by variations in a bulk parameter without closing the bulk gap. This presents a challenge in establishing a direct bulk-boundary correspondence, as conventional bulk invariants change only upon the closure of the bulk gap. Our study of two-dimensional higher-order phases in DIII and BDI symmetry classes, both characterized by chiral symmetry, demonstrates that Fermi level crossings facilitate a direct connection between the bulk Hamiltonian and Majorana zero modes at corners. These crossings, emerging as boundary conditions vary, can be identified from the bulk Hamiltonian. For both classes, we introduce a pair of topological invariants derived from these Fermi level crossings to characterize the higher-order topology. Phases in which at least one invariant assumes a nonzero value are anticipated to host Majorana corner modes. Moreover, these invariants may change with the closure of either bulk or edge gaps, thereby providing a clear and direct demonstration of bulk-boundary correspondence in higher-order phases. Our findings offer a promising framework for systematically exploring higher-order topology through boundary condition modulation.

I. INTRODUCTION

Topology in superconducting systems is typically characterized by invariants derived from bulk states under the assumption of periodic boundary condition (PBC) [1, 2]. In most scenarios, a nontrivial topological invariant guarantees the emergence of localized Majorana modes [3–10] at the boundaries (edges or surfaces), which are introduced by “cutting” the periodic system. This phenomenon, known as bulk-boundary correspondence, is a defining feature of topological states of matter. The recognition of higher-order topology [11–17] extends this correspondence, leading to the expectation that Majorana modes in superconductors may also appear at intersections (corners or hinges) of adjacent boundaries. This implies that a nontrivial higher-order topological superconductor [18–26] manifests Majorana modes when cut at least twice along different directions. While this higher-order extension broadens the potential material base within the topological family, it also presents challenges in fully understanding the connection between bulk properties and boundary signatures.

A pertinent question is whether one may identify topologically protected Majorana modes directly from the bulk Hamiltonian in higher-order topological superconductors. The answer to this question becomes nuanced when considering the influence of crystalline symmetries. It’s well known that crystalline symmetry, such as mirror symmetry, can protect higher-order topology unless the bulk gap closes [27]. States exhibiting this characteristic are termed intrinsic higher-order topological states [28], resembling topological crystalline states, wherein characterizing nontrivial topology from the bulk states of a periodic system, using symmetry indicators for instance [29–40], is plausible. However, higher-order states also distinguish themselves from topological crystalline states in that their boundary signatures can persist even un-

der perturbations breaking related crystalline symmetries [41–45]. In this circumstance, variations in a bulk parameter may drive the system across topological phase transitions without closing the bulk gap, making it a challenging task to establish a direct bulk-boundary correspondence.

In our previous work [46] on two-dimensional (2D) superconductors in the D symmetry class, we discovered that Fermi level crossings — zero-energy band crossings in the energy spectrum — serve as robust indicators for higher-order topology. These crossings manifest as the 2D system transitions from toroidal to cylindrical geometry. Topological phases transitions, occurring where either the bulk or edge gap closes, are accompanied with the emergence or disappearance of Fermi level crossings. Importantly, these crossings could be readily identified from bulk Hamiltonian, thereby acting as a bridge connecting the bulk Hamiltonian and Majorana corner modes. In this study, we focus on the DIII and BDI symmetry classes, and examine the higher-order bulk-boundary correspondence within the same framework. In contrast to the D class, the topological charges associated with these crossings — well defined due to the presence of chiral symmetry in the two classes — also play a pivotal role in determining the higher-order topological invariants.

The rest of this article is organized as follows: In Sec. II, we set up the general framework and introduce the boundary-modulated Hamiltonian that is central to our study. In Sec. III, we demonstrate how a pair of higher-order topological invariants, which are derived from Fermi level crossings, characterize the higher-order topology in the DIII class, and then take a specific model as an example for illustration. In Sec. IV we investigate the higher-order bulk-boundary correspondence in the BDI class following the same procedure as in the DIII class. Finally, in Sec. V we provide additional discussions

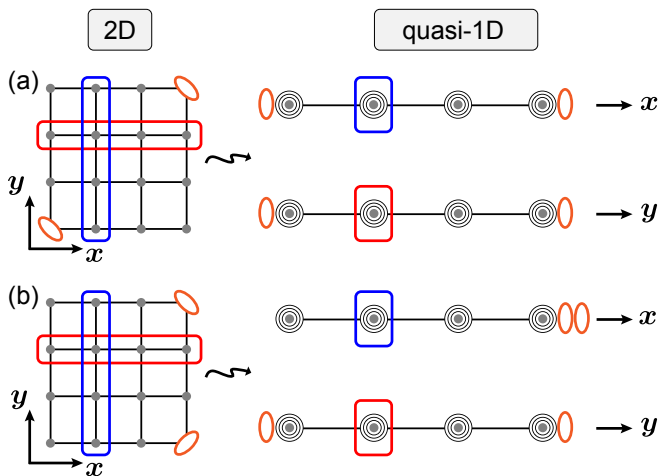


FIG. 1. Illustration of the equivalence between higher-order topology in 2D systems and first-order topology in quasi-1D systems. (a) Majorana zero modes, indicated by the orange ovals, reside at two opposite corners in the 2D system. In this configuration, the quasi-1D systems along the x and y direction both exhibit nontrivial first-order topology. (b) Majorana zero modes appear at two adjacent corners. In this scenario, only the quasi-1D system oriented along the y direction demonstrates nontrivial first-order topology. Lattice sites enclosed by blue (red) rectangles correspond to a single unit cell in the quasi-1D system extending along the x (y) direction.

and a brief summary to our work.

II. BOUNDARY-MODULATED HAMILTONIAN

We consider a generic 2D superconducting system with boundary conditions being modulated in the x or y direction [31, 47]. The Hamiltonian is composed of two parts, given by

$$\mathcal{H}_a(\lambda_a) = \mathcal{H} - (1 - \lambda_a)\mathcal{B}_a, \quad (1)$$

where $a = x(y)$ and $\bar{a} = y(x)$. The first part, \mathcal{H} , represents the bulk Hamiltonian, describing a system with periodic boundary condition in both directions. The second part, \mathcal{B}_a , introduces boundary terminations and is referred to as *boundary Hamiltonian*. \mathcal{B}_a includes all inter-cell terms crossing the terminations (edges) that extend along the \bar{a} direction. It is important to note that this definition of the boundary Hamiltonian does not involve intra-cell terms on boundary sites. In this paper, we only consider boundary terminations that are commensurate with unit cells. As such, the boundary Hamiltonian can be readily inferred from the bulk Hamiltonian. The real parameter λ_a controls the boundary condition in the a direction and modulates only the amplitude of the boundary Hamiltonian. In particular, $\lambda_a = 1(0)$ corresponds to periodic (open) boundary condition, with $\mathcal{H}_a(\lambda_a = 1(0))$ describing a toroidal (cylindrical) system. Varying λ_a

continuously in the range $[0, 1]$ is akin to gradually cutting the periodic system along the \bar{a} direction.

For the boundary-modulated Hamiltonian \mathcal{H}_a , the momentum along the \bar{a} direction remains a good quantum number, allowing us to express its second-quantized form as

$$\mathcal{H}_a(\lambda_a) = \sum_{k_{\bar{a}}} \Psi_a^\dagger(k_{\bar{a}}) H_a(k_{\bar{a}}, \lambda_a) \Psi_a(k_{\bar{a}}), \quad (2)$$

where $\Psi_a(k_{\bar{a}})$ is the Nambu spinor, and $H_a(k_{\bar{a}}, \lambda_a)$ is the Bloch Bogoliubov-de Gennes (BdG) Hamiltonian, defined in the space parameterized by $(k_{\bar{a}}, \lambda_a)$, with $k_{\bar{a}} \in [-\pi, \pi)$ and $\lambda_a \in [0, 1]$. We may alternatively view \mathcal{H}_a as a series of quasi-one dimensional (1D) Hamiltonian with varying λ_a , which all extend along the \bar{a} direction, as depicted in Fig. 1. The unit cell for this quasi-1D system has a dimension proportional to the number of lattice sites in the a direction. This boundary-modulated Hamiltonian is central to our study of higher-order topology in both symmetry classes. Unless otherwise stated, we will omit the subscript of $k_{\bar{a}}$ and λ_a , with the understanding that the Bloch Hamiltonian $H_a(k, \lambda)$ is defined in the $(k_{\bar{a}}, \lambda_a)$ parameter space.

To determine the higher-order topology, we begin with the cylindrical Hamiltonian $\mathcal{H}_a(\lambda = 0)$, which features two edges stretching along the \bar{a} direction. When the 2D system supports Majorana corner modes, distributed as in Fig. 1, the quasi-1D cylindrical system exactly resembles a nontrivial first-order topological superconductor in 1D, with stable Majorana zero modes at its ends. In this case, we may directly apply the topological invariants used for diagnosing first-order topology to the cylindrical system. When assuming nontrivial values, these invariants indicate Majorana zero modes emerging at the corners, formed by cutting the cylindrical system along the direction perpendicular to its edges. As the invariants are derived from cylindrical Hamiltonian, they fail to reveal the connection between Majorana corner modes and the 2D bulk (toroidal) Hamiltonian. To explore the bulk-boundary correspondence in higher-order phases, we shall investigate how the boundary-modulated Hamiltonian responds to the continuously varying λ .

In our previous study of D-class superconductors, we established that Fermi level crossings, which emerge during variations of λ , could be utilized to identify nontrivial higher-order phases. For a D-class system, it suffices to consider Fermi level crossings on the high-symmetry lines, namely $K = 0$ and π , in the (k, λ) parameter space. The higher-order topology is characterized by a pair of \mathbb{Z}_2 invariants, denoted as $(\mathcal{M}_x, \mathcal{M}_y)$, which relates to the total count of Fermi level crossings. When either of these invariants assumes the value -1 , the system is anticipated to harbor Majorana corner states, as depicted in Fig. 2(a). In this article, we focus on the DIII and BDI symmetry classes, and aim to demonstrate that, Fermi level crossings emerging at any point in the parameter space may significantly influence the higher-order topology in these classes. The topological invariants are deter-

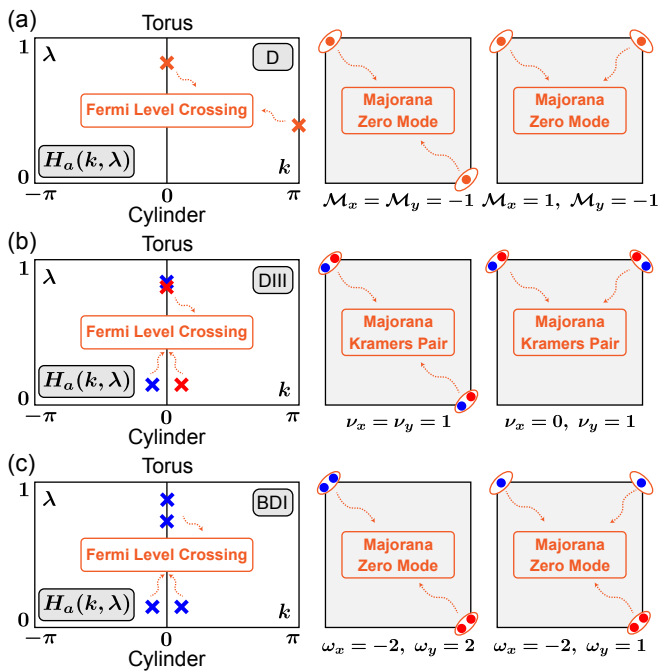


FIG. 2. Fermi level crossings in nontrivial higher-order phases of three symmetry classes. Higher-order topology in each class is characterized by a pair of topological invariants. (a) In the D class, only the crossings (marked by orange crosses) on high-symmetry lines contribute to the \mathbb{Z}_2 type topological invariants ($\mathcal{M}_x, \mathcal{M}_y$). (b) In the DIII class, Fermi level crossings occur in pairs at $(\pm k_F, \lambda_F)$, with each pair possessing opposite topological charges, indicated by crosses in different colors. The system with one or both of the two \mathbb{Z}_2 invariants (ν_x, ν_y) taking nonzero values is expected to support Majorana Kramers pairs at corners. (c) In the BDI class, Fermi level crossings off high-symmetry lines appear in pairs at $(\pm k_F, \lambda_F)$. Unlike in the DIII class, the two crossings in each pair may not have opposite topological charges. The higher-order topological invariants (ω_x, ω_y) in this class are of \mathbb{Z} type. In panels (b) and (c), the colors of the dots indicate the chiralities (± 1) of Majorana zero modes.

mined by the cumulative topological charges of all crossings.

III. DIII CLASS

In the tenfold classification scheme [2], a DIII-class system is characterized by three intrinsic symmetries, namely time-reversal (T), particle-hole (P) and chiral symmetry (S). They act on the Hamiltonian $H_a(k, \lambda)$ according to

$$\begin{aligned} TH_a(k, \lambda)T^{-1} &= H_a(-k, \lambda), & T^2 &= -1 \\ PH_a(k, \lambda)P^{-1} &= -H_a(-k, \lambda), & P^2 &= 1 \\ SH_a(k, \lambda)S^{-1} &= -H_a(k, \lambda), & S^2 &= 1 \end{aligned} \quad (3)$$

where T and P are anti-unitary operators and S is a unitary operator. From Eq.(3) we observe that time-reversal

and particle-hole transformations act as reflections in the (k, λ) parameter space, with the high-symmetry lines at $K = 0, \pi$ serving as the mirror lines. As a result, each crossing at (k_F, λ_F) has its partner at $(-k_F, \lambda_F)$. Additionally, chiral symmetry enforces that zero energy levels at any point in the parameter space are degenerate, with the degeneracy being $2n$, where n represents the number of Fermi level crossings at that point. On the high-symmetry lines, if Fermi level crossings exist, they are anticipated to come in pairs due to Kramers degeneracy, thereby ensuring that the total count of Fermi level crossings on these lines is always even. In D-class systems, the parity of this number is closely related to the higher-order topological invariant \mathcal{M}_a . The emergence of Majorana corner states is expected when the parity is odd, i.e., \mathcal{M}_x or \mathcal{M}_y equals -1 , as illustrated in Fig. 2(a). Apparently, these invariants always take trivial values in DIII-class systems, and hence could not be used to characterize the higher-order topology therein. In our subsequent discussions, we introduce a pair of \mathbb{Z}_2 invariants, which also relate to Fermi level crossings, to diagnose the nontrivial higher-order topology of the DIII class.

A. \mathbb{Z}_2 invariants

Following the same procedure as in the D class, we relate the higher-order topology in the 2D system to the first-order topology of the corresponding cylindrical Hamiltonian $\mathcal{H}_a(0)$, which describes a quasi-1D system with periodic boundary condition in the \bar{a} direction. Due to Kramers degeneracy, Majorana zero modes are always paired in real space, forming Majorana Kramers pairs. When such pairs manifest at two of the four corners in a square sample, as shown in Figs. 1 and 2(b), we can expect the quasi-1D system, extending along the x or y direction, to exhibit nontrivial first-order topology. In DIII class, the first-order topology is characterized by topological invariants of \mathbb{Z}_2 type.

To further our analysis, we note that the Bloch BdG Hamiltonian $H_a(k, \lambda)$ can be transformed into an off-diagonal form in the eigenbasis of the chiral symmetry operator. This is represented by

$$U_S^\dagger H_a(k, \lambda) U_S = \begin{pmatrix} 0 & D_a(k, \lambda) \\ D_a^\dagger(k, \lambda) & 0 \end{pmatrix}, \quad (4)$$

where U_S is the unitary matrix that diagonalizes chiral symmetry operator S . For the DIII class, with an appropriate selection of U_S , the D matrix in Eq.(4) can always be written in a form that satisfies $D_a(k, \lambda) = -D_a^T(-k, \lambda)$ [48], implying that the D matrix on high-symmetry lines, $D_a(K, \lambda)$, is antisymmetric. Employing singular value decomposition, we write $D_a(k, \lambda) = U_a(k, \lambda)\Lambda_a(k, \lambda)V_a^\dagger(k, \lambda)$, where U_a and V_a are both unitary matrices, and Λ_a is a diagonal matrix with non-negative entries. We then define a unitary q matrix, $q_a(k, \lambda) = U_a(k, \lambda)V_a^\dagger(k, \lambda)$. The first-order topology of the quasi-1D Hamiltonian $\mathcal{H}_a(\lambda)$ is characterized by

topological invariant $\tilde{\nu}_a(\lambda)$ in terms of the q matrix [49], which reads

$$(-1)^{\tilde{\nu}_a(\lambda)} = \frac{\text{Pf}[q_a(0, \lambda)]}{\text{Pf}[q_a(\pi, \lambda)]} \frac{\sqrt{\det[q_a(\pi, \lambda)]}}{\sqrt{\det[q_a(0, \lambda)]}} = \frac{\text{Pf}[q_a(0, \lambda)]}{\text{Pf}[q_a(\pi, \lambda)]} \times \exp \left\{ \frac{1}{2} \int_0^\pi dk \partial_k \ln \det[q_a(k, \lambda)] \right\}, \quad (5)$$

where ‘‘Pf’’ represents Pfaffian. In Eq.(5), $\sqrt{\det[q_a(k, \lambda)]}$ is required to be in the same branch for $k \in [0, \pi]$. Notably, $\tilde{\nu}_a(0)$ and $\tilde{\nu}_a(1)$ represent the first-order topological invariants of cylindrical and toroidal systems, respectively. We denote $\nu_a = \tilde{\nu}_a(0)$, and the pair of invariant, (ν_x, ν_y) , can precisely characterize nontrivial higher-order phases. Specifically, when either ν_x or ν_y equals 1, the 2D system is expected to host two Majorana Kramers pairs distributed at two corners, as shown in Fig. 2(b). Alternatively, utilizing the two equalities, $\text{Pf}(D_a) = \sqrt{|\det(D_a)|} \text{Pf}(q_a)$ and $\det(D_a) = |\det(D_a)| \det(q_a)$, the topological invariants can also be expressed using the D matrix, which reads

$$(-1)^{\tilde{\nu}_a(\lambda)} = \frac{\text{Pf}[D_a(0, \lambda)]}{\text{Pf}[D_a(\pi, \lambda)]} \frac{\sqrt{\det[D_a(\pi, \lambda)]}}{\sqrt{\det[D_a(0, \lambda)]}} = \frac{\text{Pf}[D_a(0, \lambda)]}{\text{Pf}[D_a(\pi, \lambda)]} \times \exp \left\{ \frac{1}{2} \int_0^\pi dk \partial_k \ln \det[D_a(k, \lambda)] \right\}. \quad (6)$$

Equations (5) and (6), both formulated using cylindrical Hamiltonian $H_a(0)$, do not elucidate the link between corner modes and bulk Hamiltonian. To achieve this, our subsequent analysis aims to connect the pair of invariants to the Fermi level crossings that occur as the parameter λ varies. These crossings can be derived from bulk Hamiltonian of the 2D system, thus allowing us to establish a direct bulk-boundary correspondence in higher-order phases.

B. Fermi level crossings

Before delving into the relationship between Fermi level crossings and higher-order topological invariants, we first take a look at the physical meaning of $\tilde{\nu}_a(1)$, which is associated with the torus Hamiltonian $\mathcal{H}_a(1)$. When interpreting the torus system as a quasi-1D system along the \bar{a} direction, a nontrivial $\tilde{\nu}_a(1)$ implies the presence of Majorana Kramers pairs at both ends. This translates to the existence of gapless Majorana modes propagating along the edges in the a direction of the 2D system, a feature of first-order topological superconductors in DIII class. However, our interest lies in topological superconductors that exhibit nontrivial higher-order topology while maintaining trivial first-order topology, characterized by gapped edge spectra. Therefore, in our context, $\tilde{\nu}_a(1)$ is always assumed to be zero. This suggests that, in the nontrivial higher-order phase, the \mathbb{Z}_2 invariant $\tilde{\nu}_a(\lambda)$ is expected to change at some point as λ is continuously

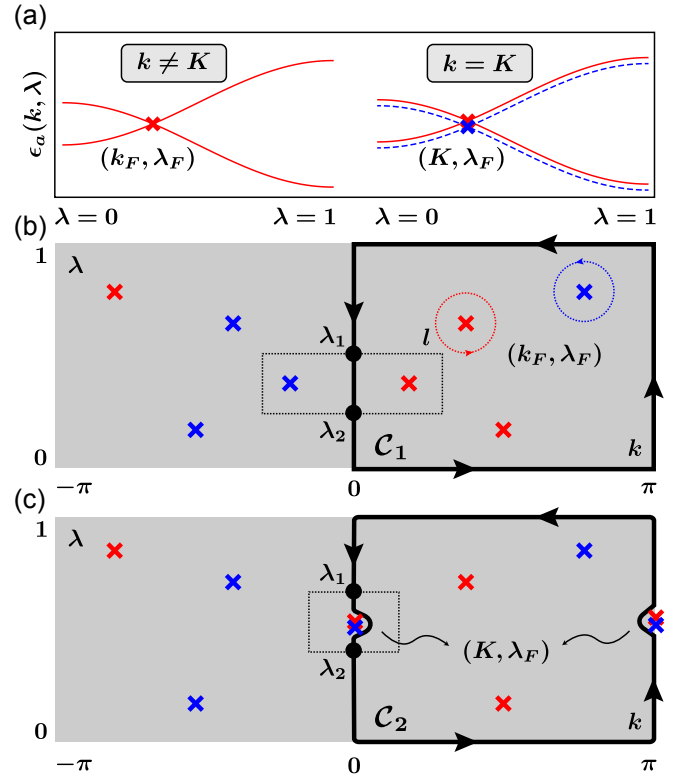


FIG. 3. Fermi level crossings on and off high-symmetry lines in DIII class. (a) Variations of energy spectra with λ for fixed k . On high-symmetry lines (right panel), Kramers degeneracy requires all energy levels to be degenerate and hence Fermi level crossings always come in pairs, whereas there is no such restriction for the crossings off high-symmetry lines (left panel). The red (solid) and blue (dashed) lines are deliberately shifted for demonstration of the degeneracy. (b) The first case where the crossings only occur off high-symmetry lines. (c) The second case with crossings on high-symmetry lines. The loop \mathcal{C}_2 now excludes these crossings. The red and blue crosses indicate Fermi level crossings with opposite topological charges. A \mathbb{Z}_2 topological charge can be associated to each pair of crossings, by considering a loop (black dashed lines in (b) and (c)) that encloses the pair of crossings.

varied from 1 to 0. This transition point is exactly where Fermi level crossings occur. In this regard, Fermi level crossings reveal the topological distinctions between the toroidal and the cylindrical system, which is crucial to our understanding of the bulk-boundary correspondence in higher-order topological phases.

Combining the expression of $\tilde{\nu}_a(\lambda)$ for $\lambda = 0$ and $\lambda = 1$ from Eq.(6), we arrive at an equivalent formula for the higher-order topological invariant ν_a , namely $\tilde{\nu}_a(0)$, which is given by

$$(-1)^{\nu_a} = \frac{\text{Pf}[D_a(0, 0)] \text{Pf}[D_a(\pi, 1)]}{\text{Pf}[D_a(0, 1)] \text{Pf}[D_a(\pi, 0)]} \times \exp \left\{ \frac{1}{2} \int_0^\pi dk \partial_k \ln \frac{\det[D_a(k, 0)]}{\det[D_a(k, 1)]} \right\}. \quad (7)$$

Our next step is to show that the ratio of Pfaffian terms in

Eq.(7) can be reformulated as an integral. It is important to note that while the D matrix on high-symmetry lines ($K = 0$ or π), denoted as $D_a(K, \lambda)$, is well defined for all $\lambda \in [0, 1]$, its determinant may become zero. Following this observation, our subsequent analysis will distinguish between two cases.

In the first case, we assume $\det[D_a(K, \lambda)] \neq 0$ for all values of λ , indicating that there are no Fermi level crossings on the high-symmetry lines. We then select N_λ equally spaced points along these lines, with $\lambda_n = n/N_\lambda$ for integers n in the range $[0, N_\lambda]$. This allows us to express the ratio of Pfaffians in Eq.(7) as the product of ratios for adjacent points, which reads

$$\frac{\text{Pf}[D_a(K, 1)]}{\text{Pf}[D_a(K, 0)]} = \prod_{n=0}^{N_\lambda-1} \frac{\text{Pf}[D_a(K, \lambda_{n+1})]}{\text{Pf}[D_a(K, \lambda_n)]} \quad (8)$$

Under the condition that $\det[D_a(K, \lambda)] \neq 0$, the phase of $\text{Pf}[D_a(K, \lambda)]$ can be made to vary continuously with λ , and so is the phase of $\sqrt{\det[D_a(K, \lambda)]}$. Due to this continuity we have

$$\frac{\text{Pf}[D_a(K, \lambda_{n+1})]}{\text{Pf}[D_a(K, \lambda_n)]} = \frac{\sqrt{\det[D_a(K, \lambda_{n+1})]}}{\sqrt{\det[D_a(K, \lambda_n)]}}. \quad (9)$$

With this equality, we may further express Eq.(8) in an integral form in the limit of infinitely large N_λ , given by

$$\frac{\text{Pf}[D_a(K, 1)]}{\text{Pf}[D_a(K, 0)]} = \exp \left\{ \frac{1}{2} \int_0^1 d\lambda \partial_\lambda \ln \det[D_a(K, \lambda)] \right\}. \quad (10)$$

From Eq.(10) it follows that the ratio of Pfaffian in the left side of Eq.(10) is related to line integrals of the determinant of D matrix along high-symmetry lines, similar to the integral in Eq.(6), which is calculated along lines with a constant λ in the parameter space. Substituting Eq.(10) into Eq.(7), we obtain

$$\begin{aligned} (-1)^{\nu_a} &= \exp \left\{ \frac{1}{2} \oint_{\mathcal{C}_1} dl \nabla_l \ln \det[D_a(k, \lambda)] \right\} \\ &= \exp \left[i\pi \sum_{(k_F, \lambda_F)} n_a(k_F, \lambda_F) \right], \end{aligned} \quad (11)$$

where the integration along the loop \mathcal{C}_1 , illustrated in Fig. 3(a), represents the winding number of the D matrix. In the second equality of Eq.(11), we identify the winding number as the sum of topological charges for all Fermi level crossings (k_F, λ_F) enclosed by \mathcal{C}_1 , with $n_a(k_F, \lambda_F)$ representing the corresponding charge. In practice, n_a is determined by calculating the winding number along a loop that encloses the crossing, such as the circle l in Fig. 3(b). Time-reversal symmetry guarantees that each crossing at (k_F, λ_F) has its partner at $(-k_F, \lambda_F)$. Due to the relation $D_a(k_F, \lambda_F) = -D_a(-k_F, \lambda_F)^T$, the two partners have opposite charges, i.e., $n_a(k_F, \lambda_F) = -n_a(-k_F, \lambda_F)$. Thus, the total topological charges of

Fermi level crossings on either half of the parameter space could give the same ν_a .

Now let us consider the second case, where Fermi level crossings also occur on high-symmetry lines. Considering that Pfaffian of the D matrix becomes zero at the crossing (K, λ_F) , we need to exclude them while selecting the sample points in Eq.(8). Also, Eq.(9) may fail if there exists crossings between the two adjacent points, which we denote as $(K, \lambda_F \pm \delta\lambda)$. The phase difference of the Pfaffian between these two points is not necessarily infinitely small while $\delta\lambda$ approaches zero. In this case, the loop \mathcal{C}_1 in Eq.(11) is replaced by \mathcal{C}_2 shown in Fig. 3(b), which exactly circumvents the crossings. All the sample points still lie on the high-symmetry lines. On the vertical line segments of \mathcal{C}_2 , $\sqrt{\det[D_a(k, \lambda)]}$ can be made to vary continuously, thus ensuring $\sqrt{\det[D_a(K, \lambda_F + \delta\lambda)]}/\sqrt{\det[D_a(K, \lambda_F - \delta\lambda)]}$ to be infinitely small. This leads to the relation

$$\begin{aligned} \frac{\text{Pf}[D_a(K, \lambda_F + \delta\lambda)]}{\text{Pf}[D_a(K, \lambda_F - \delta\lambda)]} &= (-1)^{\eta_a(K, \lambda_F)} \\ &\times \frac{\sqrt{\det[D_a(K, \lambda_F + \delta\lambda)]}}{\sqrt{\det[D_a(K, \lambda_F - \delta\lambda)]}}, \end{aligned} \quad (12)$$

where $\eta_a(K, \lambda_F)$ is an integer that depends on the crossing at (K, λ_F) . Comparing with Eq.(9), there is an additional phase factor in Eq.(12). An odd η_a suggests a π -phase shift in $\text{Pf}[D_a(K, \lambda)]$ across the Fermi level crossings.

In order to determine the precise value of η_a , we decompose the $2N \times 2N$ antisymmetric matrix $D_a(K, \lambda)$ into the form $D_a = Q_a^T M_a Q_a$, with Q_a being a unitary matrix, and M_a taking the block diagonal form as follows,

$$M_a = \text{diag} \left\{ \begin{pmatrix} 0 & m_{a,1} \\ -m_{a,1} & 0 \end{pmatrix}, \dots, \begin{pmatrix} 0 & m_{a,N} \\ -m_{a,N} & 0 \end{pmatrix} \right\}. \quad (13)$$

For a non-singular D matrix, $\pm m_{a,j}$, which represent eigenvalues of Hamiltonian $\mathcal{H}_a(K, \lambda)$, all take finite values. Assuming $|m_{a,1}|$ to be the smallest nonnegative energy level near the crossing (K, λ_F) , we then have $m_{a,1} = 0$ exactly at the crossing. In the case of linear band crossing, we have $m_{a,1} \propto (\lambda - \lambda_F)$ near the crossing. As λ crosses λ_F , a level crossing occurs between $m_{a,1}$ and $-m_{a,1}$, as Fig. 3(a) shows in the energy spectrum, and hence $m_{a,1}$ is expected to change its sign. We should note that, there are two degenerate crossings in the energy spectrum due to Kramers degeneracy, but $\pm m_{a,j}$ in Eq.(13) only account for half of the energy levels. While λ crosses λ_F , Q_a — specifically, the phase of its determinant — changes continuously. Alternatively, one may require $m_{a,1}$ to remain nonnegative, by swapping the positions of $\pm m_{a,1}$ in Eq.(13) after crossing λ_F , albeit at the expense of altering the sign of $\det[Q_a]$. Here, to clarify how Fermi level crossings affect the Pfaffian of D matrix, we require $\det[Q_a]$ to be a continuous function of λ near the crossing. By expressing the Pfaffian of D

matrix as

$$\text{Pf}[D_a(K, \lambda)] = \det[Q_a(K, \lambda)] \prod_{j=1}^N m_{a,j}(K, \lambda), \quad (14)$$

we readily find that the sign change of $m_{a,1}$ leads to an abrupt π -phase shift in the Pfafian of D matrix. At λ_F , it's possible for more than one pair of $\pm m_{j,a}$ to cross zero energy. The number of such pairs is precisely half that of zero singular values of $D_a(K, \lambda_F)$ if we only consider linear band crossings. According to Eq.(12), each pair contributes to a π -phase shift, and hence this number is also equal to $\eta_a(K, \lambda_F)$. Since only the parity of η_a matters, we may define the parity of η_a to be the \mathbb{Z}_2 charge of the crossing pair on the high-symmetry lines. In this case, Eq.(8) still holds, as the sample points λ_n do not include the crossing points. For the two sample points adjacent to the crossing, Eq.(9) needs to be replaced by Eq.(12). It then follows from Eq.(7) that, the higher-order topological invariant in the second case is given by

$$(-1)^{\nu_a} = \prod_{(K, \lambda_F)} (-1)^{\eta_a(K, \lambda_F)} \times \exp \left[i\pi \sum_{(k_F \neq K, \lambda_F)} n_a(k_F, \lambda_F) \right]. \quad (15)$$

Comparing with Eq.(11), Eq.(15) also includes contributions from Fermi level crossings on high-symmetry lines. The summation in the second line of Eq.(15) involves crossings in either half of the parameter space.

In both cases aforementioned, the pair of higher-order topological invariants (ν_x, ν_y) are determined by the topological charges of Fermi level crossings in the parameter space. For the crossings off the high-symmetry lines, their topological charges, n_a , are of \mathbb{Z} type, in contrast to the \mathbb{Z}_2 charge, namely η_a , for crossings on the high-symmetry lines. Although n_a may take any integer values, the topological invariants only depend on its parity, as Eq.(11) and (15) suggests. Besides, the time-reversal partner of each crossing actually doesn't provide additional information. With these observations, we may treat each pair of Fermi level crossings at $(\pm k_F, \lambda_F)$ as a whole, and associate a \mathbb{Z}_2 charge to them in a unified fashion, regardless of whether they appear on or off the high-symmetry lines. The topological charge, denoted as $\tilde{n}_a(k_F, \lambda_F)$, is defined according to [48]

$$(-1)^{\tilde{n}_a(k_F, \lambda_F)} = \frac{\text{Pf}[D_a(K, \lambda_1)] \sqrt{\det[D_a(K, \lambda_2)]}}{\text{Pf}[D_a(K, \lambda_2)] \sqrt{\det[D_a(K, \lambda_1)]}}, \quad (16)$$

where the two points, (K, λ_1) and (K, λ_2) , are the intersections of the high-symmetry line and the dashed square loop, as depicted in Figs. 3(b) and (c). The loop encloses only the pair of Fermi level crossings considered. In Eq.(16), $\sqrt{\det[D_a(k, \lambda)]}$ is required to vary continuously along the left or right half of the loops, instead on the high-symmetry lines, where Fermi level crossings may

appear. Equation (16) reduces to Eq.(12) when considering an infinitely small loop and setting $\lambda_1 = \lambda + \delta\lambda$, $\lambda_2 = \lambda - \delta\lambda$. Winding numbers of the D matrix along these loops are always zero, but the \mathbb{Z}_2 charge defined in Eq.(16) can be nontrivial. To be specific, $\tilde{n}_a(k_F, \lambda_F) = 1$ if $\eta_a(K, \lambda_F)$ (for crossings on the high-symmetry lines) or $n_a(k_F, \lambda_F)$ (for crossings off high-symmetry lines) is odd; otherwise $\tilde{n}_a(k_F, \lambda_F) = 0$. Consequently, the higher-order topological invariant ν_a simply reflects the parity of the total \mathbb{Z}_2 charges for all pairs of Fermi level crossings, i.e.

$$\nu_a = \sum_{(k_F \geq 0, \lambda_F)} \tilde{n}_a(k_F, \lambda_F) \text{ mod } 2. \quad (17)$$

C. Bulk-boundary correspondence

Having related the Fermi level crossings to higher-order topology, we now demonstrate how these crossings and their topological charges are effectively identified from the bulk Hamiltonian, so as to make a direct bulk-boundary correspondence in higher-order phases. This approach is applicable to systems in both DIII and BDI classes.

To begin with, we note that at the crossing point (k_F, λ_F) , λ_F is a root of characteristic equation $\det[H_a(k, \lambda)] = 0$ [50]. Its multiplicity is even due to the presence of chiral symmetry. In terms of D matrix, the characteristic equation reduces to

$$\det[D_a(k, \lambda)] = 0, \quad (18)$$

except that the root's multiplicity is halved. In particular, for linear crossings on the high-symmetry lines, we have $\det[D_a(K, \lambda)] \propto (\lambda - \lambda_F)^{p_a}$ near the crossing, from which it follows that the root's multiplicity p_a is equal to the number of zero singular values of $D_a(K, \lambda_F)$ ($\pm m_{a,1}$ in Eq.(13)), which exactly equals to $2\eta_a(K, \lambda_F)$, i.e., $p_a/2 = \eta_a$. Hence, the root's multiplicity determines the \mathbb{Z}_2 charge of Fermi level crossings on the high-symmetry lines. It's possible that the crossings are of quadratic or cubic type, and there may exist a number of crossings with different types at the same point λ_F . We will discuss this generic case in Sec. V, where it is demonstrated that the \mathbb{Z}_2 charge is still given by the parity of $p_a/2$.

Following Eq.(11), the topological charge for each individual crossing off the high-symmetry lines is equal to the winding number of the D matrix along a loop that encloses the crossing. No matter where the crossings occur, we need to compute the determinant of the D matrix. To demonstrate how it is obtained from the bulk Hamiltonian, we first write down $H_a(k, \lambda)$ as

$$H_a(k, \lambda) = H_a(k, 1) - (1 - \lambda)B_a(k), \quad (19)$$

in the Bloch basis $\Psi_a(k)$, with $B_a(k)$ being the Bloch Hamiltonian of boundary Hamiltonian \mathcal{B}_a in Eq.(1). We

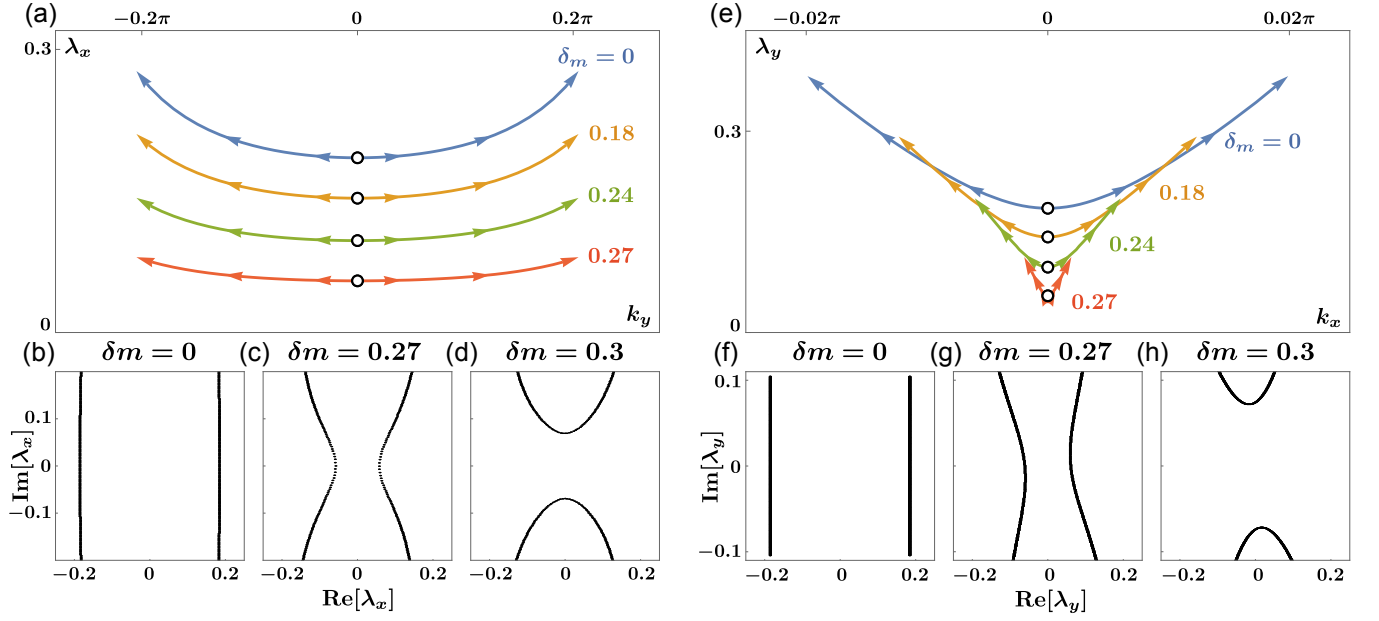


FIG. 4. The flow of Fermi level crossings in the parameter space under the variations of δm and m_1 . (a) In the (k_y, λ_x) space, a pair of crossings, marked as black circles, reside on the high-symmetry line $K = 0$ when $m_1 = 0$. Finite m_1 separates the pair and drive them off the line in opposite directions, as indicated by the arrows. With the increase of δm , the crossings move towards $\lambda = 0$ and vanish. (b)-(d) λ profiles generated by solving Eq.(24) for $k \in [-\pi, \pi)$. For sufficiently large δm , the characteristic equation has no real root, signaling the disappearance of Fermi level crossings. (e)-(h) A similar phenomenon is observed in the (k_x, λ_y) space. The other parameters are set as $\mu = 3t$, $\Delta = t$, $m = 0.4t$, $\theta = \pi/4$, which, unless otherwise specified, remain the same in subsequent plots.

denote the components of $\Psi_a(k)$ as $[c_a(k)]_{i\alpha}$, where the Latin letter i labels the unit cell along the a direction and the Greek letter α labels the degree of freedom within each cell. The entries of the Bloch Hamiltonian matrix are thus represented by $[H_a(k, \lambda)]_{i\alpha, j\beta}$. Since chiral symmetry operates within the inner space, the corresponding D matrix has a similar relation as Eq.(19), which reads

$$D_a(k, \lambda) = D_a(k, 1)A_a(k, \lambda), \quad (20)$$

with

$$A_a(k, \lambda) = \mathbb{1} - (1 - \lambda)D_a^{-1}(k, 1)D_a^b(k). \quad (21)$$

Here, $\mathbb{1}$ represents the identity matrix, and $D_a^b(k)$ is the D matrix of $B_a(k)$.

For higher-order phases with gapped bulk spectrum, $\det[D_a(k, 1)]$ always takes a finite value, and hence Eq.(18) is equivalent to

$$\det[A_a(k, \lambda)] = 0. \quad (22)$$

The boundary Hamiltonian $B_a(k)$ only involves boundary degrees of freedom, which we denote by $i_b\alpha$. Consequently, the only possible nonzero entries of $B_a(k)$ are $[B_a(k_{\bar{a}})]_{i_b\alpha, j_b\beta}$. As such, we demonstrate in Appendix A that $\det[A_a(k, \lambda)]$ is equal to the determinant of a $r_a \times r_a$ matrix, denoted by $\tilde{A}_a(k, \lambda)$, with r_a representing the

rank of $D_a^b(k)$. The specific form of $\tilde{A}_a(k, \lambda)$ is given by

$$\begin{aligned} \tilde{A}_a(k_{\bar{a}}, \lambda_a) &= \mathbb{1}_{r_a \times r_a} - \frac{1}{2\pi}(1 - \lambda_a) \\ &\times \int dk_a \tilde{V}_a^{b\dagger}[F(k_a) \otimes D^{-1}(\mathbf{k})]\bar{D}_a^b(k_{\bar{a}})\tilde{V}_a^b, \end{aligned} \quad (23)$$

where we recover the subscripts of k and λ to avoid confusion. In Eq.(23), $F(k_a)$ is related to Fourier transformation with $[F(k_a)]_{i_b, j_b} = e^{ik_a(i_b - j_b)}$, $D(\mathbf{k})$ is the D matrix of bulk Hamiltonian in 2D momentum space, and $\bar{D}_a^b(k_{\bar{a}})$ is the block that corresponds to boundary cells in matrix $D_a^b(k_{\bar{a}})$. \tilde{V}_a^b is a semi-unitary matrix related to compact singular value decomposition of $\bar{D}_a^b(k_{\bar{a}})$.

As a result, Eq.(22) reduces to

$$\det[\tilde{A}_a(k, \lambda)] = 0. \quad (24)$$

The loop integral in Eq.(15) may also be reexpressed in terms of $\tilde{A}_a(k, \lambda)$, by noting that with trivial first-order topology we always have

$$\oint_{\mathcal{C}} dl \nabla_l \ln \det[D_a(k, 1)] = 0 \quad (25)$$

for any loop \mathcal{C} in the parameter space. The topological charge of each Fermi level crossing is then determined according to

$$n_a(k_F, \lambda_F) = \frac{1}{2\pi i} \oint_{\mathcal{C}} dl \nabla_l \ln \det[\tilde{A}_a(k, \lambda)], \quad (26)$$

with \mathcal{C} being any loop that encloses the crossing (k_F, λ_F) only. Therefore, all calculations involving the determinant of $D_a(k, \lambda)$ can now be replaced by that of $\tilde{A}_a(k, \lambda)$, which, according to Eq.(23), is obtained from the D matrix of bulk Hamiltonian, $D(\mathbf{k})$. After finding all the Fermi level crossings and their topological charges, we immediately obtain the topological invariants according to Eq.(15).

So we have established that Fermi level crossings serve as a bridge that connects bulk Hamiltonian and Majorana corner modes. Although Fermi level crossings are determined from the bulk Hamiltonian, their numbers may change when bulk gap remains open. This happens when topological phases transitions are driven by the closure of edge gaps, as we shall demonstrate in the following example.

D. An example

We consider a spinful toy model in 2D with two orbital degrees in each unit cell. The Bloch BdG Hamiltonian takes the form

$$H_{\text{DIII}}(\mathbf{k}) = \epsilon_{\mathbf{k}}\tau_z + 2\Delta(\sin k_x\tau_y - \sin k_y\tau_x s_z\sigma_z) + m(\sin\theta\tau_z\sigma_x - \cos\theta s_z\sigma_y) - \delta m\tau_x s_z\sigma_y - m_1\tau_x s_x\sigma_y, \quad (27)$$

where the kinetic energy $\epsilon_{\mathbf{k}} = \mu - 2t(\cos k_x + \cos k_y)$, Δ represents the p wave pairing amplitude, and Pauli matrices τ , s and σ act in particle-hole, spin and orbital space, respectively. The three symmetry operators defined in Eq.(3) are represented as $T = -is_y\mathcal{K}$, $P = \tau_x\mathcal{K}$ and $S = \tau_x s_y$, where \mathcal{K} denotes the complex conjugation operator.

The first two terms in Eq.(27) describe two copies ($\sigma_z = \pm 1$) of topological superconductors with $p \pm ip$ pairing. Each copy features two counter-propagating helical Majorana modes on edges in the nontrivial phase. The three onsite terms m , δm and m_1 could gap out the helical modes. In particular, the m term introduces anisotropic mass gaps to the four edges, controlled by θ . This is crucial to the emergence of Majorana corner modes, which appear when two adjacent edges exhibit mass gaps of opposite signs. In the absence of m_1 , s_z is a good quantum number, and the model simply reduces to two independent copies ($s_z = \pm 1$) of the D-class model we introduced in Ref.[46]. In the D-class model, the non-trivial higher-order topology is captured by Fermi level crossings on high-symmetry lines. Crossings off these lines are not protected due to the absence of chiral symmetry. In contrast, for the DIII class, Fermi level crossings both on and off these lines contribute to the higher-order topology. Time-reversal symmetry-preserving perturbations, such as the m_1 term, either couple and eliminate the pair of crossings on high-symmetry lines or separate them away from these lines, depending on the \mathbb{Z}_2 charge of the pair defined in Eq.(16).

Given that we focus on boundary terminations commensurate with unit cells, the boundary Hamiltonian

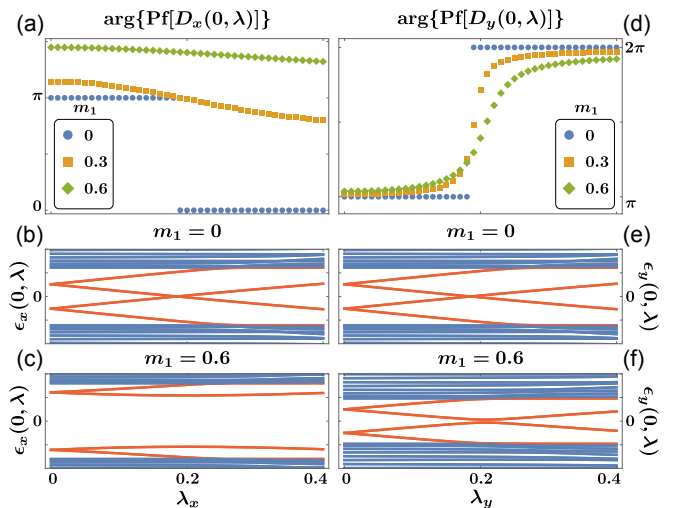


FIG. 5. The π -phase jump in Pfaffian of the D matrix induced by Fermi level crossings. (a), (d) Fermi level crossings occurring on high-symmetry lines when $m_1 = 0$ leads to an abrupt π -phase jump in $\text{Pf}[D_a(0, \lambda)]$. For cases with finite m_1 , there is no such discontinuity. (b)-(c), (e)-(f) Energy spectra along $K = 0$. No Fermi level crossing exists on the high-symmetry line when m_1 is finite. In these plots, N_a , the number of unit cells along the a direction, is chosen to be 40. The Pfaffian is calculated using the code from Ref.[51].

is directly derived from the bulk Hamiltonian. In the boundary basis, which in this model includes only the first and last unit cells — denoted as $\{\psi_{a, N_a}(k), \psi_{a, 1}(k)\}$ with N_a representing the number of unit cells in the a direction and $\psi_{a, j}(k)$ encompassing all internal degrees of freedom $[c_a(k)]_{j\alpha}$ — the resulting matrix B_a takes the following simple form,

$$B_a = \begin{pmatrix} 0 & h_a \\ h_a^\dagger & 0 \end{pmatrix} \quad (28)$$

where h_a includes all inter-cell hopping and pairing terms, with $h_x = -t\tau_z - I\Delta\tau_y$ and $h_y = -t\tau_z + I\Delta\tau_x s_z\sigma_z$. The unitary matrix that sends the bulk Hamiltonian $H(\mathbf{k})$ into block off-diagonal form is

$$U_S = \frac{1}{\sqrt{2}} \begin{pmatrix} s_0 & -is_y \\ s_y & is_0 \end{pmatrix} \otimes \sigma_0, \quad (29)$$

where s_0 and σ_0 are identity matrices in the spin and orbital space, respectively. The Fermi level crossings can then be identified according to Eqs.(23) and (24).

In Figs. 4(a) and (e), we plot the positions of Fermi level crossings in the parameter space for various values of δm and m_1 . When $m_1 = 0$, the system supports a pair of Fermi level crossings on the high-symmetry line $K = 0$. The introduction of the m_1 term drives the pair of crossings away from this line along opposite directions. The arrows in Figs. 4(a) and (e) indicate where the Fermi level crossings flow with increasing m_1 .

In this model, each Fermi level crossing at (k_F, λ_F) is also paired with another at $(k_F, -\lambda_F)$, the latter not

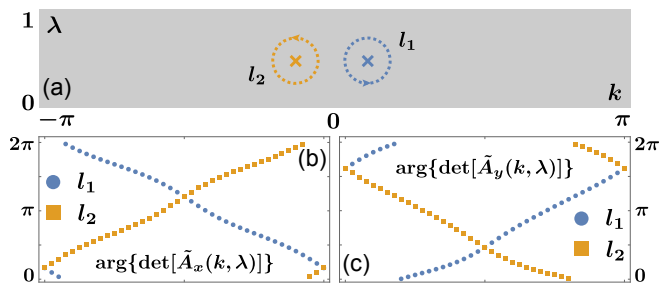


FIG. 6. Topological charges of Fermi level crossings off high-symmetry lines. Nontrivial windings in the phase of $\det[\tilde{A}_a(k, \lambda)]$ are observed along the loops l_1 and l_2 , each of which encircles a single Fermi level crossing. The two time-reversal partners at $\pm k_F$ carry opposite charges. In these plots, $m_1 = 0.3t$ and $\delta m = 0$.

explicitly shown here as we focus only on crossings with $\lambda_F \in [0, 1]$. As δm increases (see Figs. 4(a) and (e)), the crossings at $\pm \lambda_F$ migrate towards $\lambda = 0$, eventually annihilating. A straightforward way to illustrate this transition is through the λ profile, which displays all roots of Eq.(24) for $k \in [-\pi, \pi]$. Fermi level crossings correspond to real roots for λ . As depicted in Figs. 4(b)-(d) and (f)-(h), the Fermi level crossings vanish at sufficiently large δm , signaling edge phase transitions where Majorana zero modes at different corners may either change positions or couple. Our previous study in the D-class model [46] showed that, in the absence of m_1 , the energy gap on edges along the x direction closes at $|\delta m| = |m \sin \theta|$, and along the y direction at $|\delta m| = |m \cos \theta|$. The presence of m_1 term has a negligible impact on these gap-closing points. Pinpointing the phase transition position for finite m_1 is not our focus here. Instead our next step is to examine the topological charges of these Fermi level crossings in order to derive the higher-order topological invariants.

Let's first consider Fermi level crossings on high-symmetry lines, denoted as (K, λ_F) . We already know that λ_F is a root of Eq.(24) at $k = K$. According to Eq.(12), $\eta_a(K, \lambda_F)$, which equals to half the root's multiplicity, determines whether the Pfaffian of the D matrix experiences a π -phase jump as λ crosses this point. The plots corresponding to $m_1 = 0$ in Figs. 5 (a) and (c) indeed exhibit such a jump, suggesting an odd η_a . By solving Eq.(24), we obtain a real root with multiplicity 2, implying $\eta_a(K, \lambda_F) = 1$. This is consistent with the energy spectrum along the high-symmetry line in Figs. 5(b) and (e), where each level is doubly degenerate due to Kramers degeneracy, resulting in exactly two linear band crossings at the zero energy for $m_1 = 0$. Turning on m_1 drive the crossings away from the high-symmetry line, and hence the Pfaffian of D matrix varies continuously along the line, as is seen in Figs. 5(a) and (d) for finite m_1 . This leads us to the first case investigated in Sec. IIIB, where Fermi level crossings appear off the high-symmetry lines.

Since the pair of crossings on the high-symmetry line

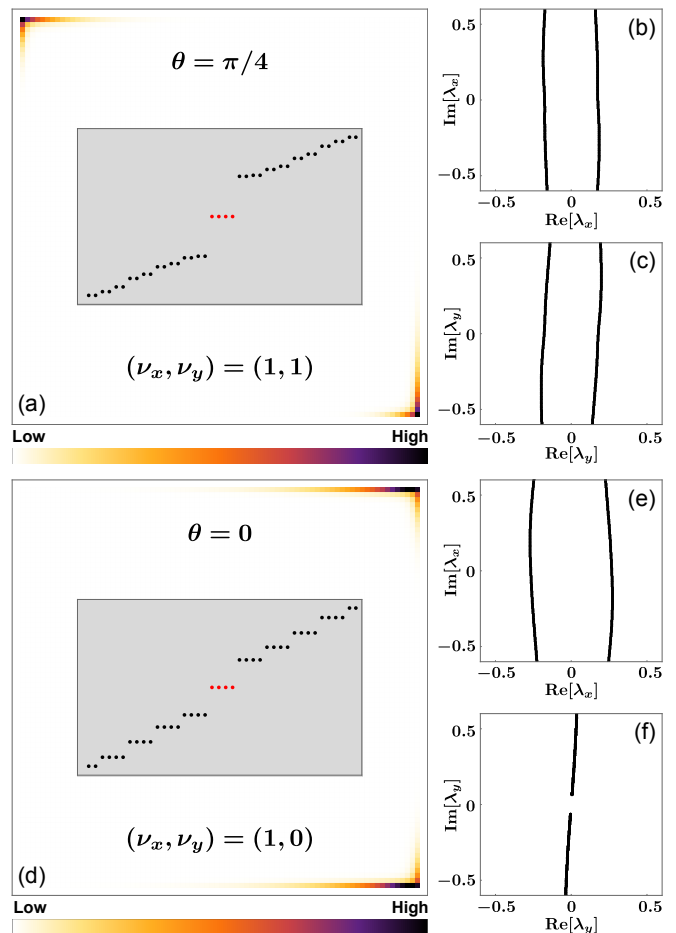


FIG. 7. Distributions of Majorana Kramer pairs in nontrivial higher-order phases. (a) The probability distributions of Majorana zero modes. The inset shows the energy spectrum for an 80×80 open-boundary system, with red dots representing Majorana zero modes. The two invariants, ν_x and ν_y , both take nontrivial values, as indicated by λ profiles in (b) and (c). This results in two Majorana Kramer pairs sitting at opposite corners. (d) Only one of the invariants is nonzero, as revealed by λ profiles in (e) and (f), and the two Majorana pairs therefore reside on adjacent corners. In these plots, $m_1 = 0.3t$ and $\delta m = 0.1t$.

has a nontrivial \mathbb{Z}_2 charge, we can expect finite m_1 doesn't couple them. To verify this argument, we may first locate the position of each crossing, followed by the determination of their topological charges according to Eq.(26). Note that each crossing at (k_F, λ_F) has its time-reversal partner at $(-k_F, \lambda_F)$, with opposite charges. In Figs. 6(b) and (c), we show the phase of $\det[\tilde{A}_a(k, \lambda)]$ along a contour that encircles each crossing for $m_1 = 0.3$, which clearly shows nontrivial windings, with topological charges being ± 1 . This suggests the \mathbb{Z}_2 charge associated with the pair of crossings remains to be 1. Due to this nontrivial \mathbb{Z}_2 charge, finite m_1 can at most separate the two crossings away from each other.

Through the analysis above, we are able to obtain the pair of topological invariants (ν_x, ν_y) as defined in

Eq.(15). For the examples shown in Figs. 5 and 6, we have $(\nu_x, \nu_y) = (1, 1)$, which indicates that two Majorana Kramers pairs sit at diagonals, as depicted in Fig. 7(a). Without inversion symmetry, the two Majorana pairs may reside at any two corners. In any of the cases, at least one of the invariants is nonzero. As showcased in Fig. 7(d) for $\theta = 0$, Fermi level crossings only occur in (k_y, λ_x) parameter space and hence $(\nu_x, \nu_y) = (1, 0)$, suggesting two Majorana Kramers pairs emerging at neighboring corners. It's important to note that when both the two invariants are zero, the system may still reside in nontrivial higher-order phases. For instance, if all four corners host Majorana Kramers pairs, both invariants are zero. Hence, when at least one of the two invariants is nonzero, we immediately know the system resides in the nontrivial higher-order phase, not the other way around. This argument also applies to the BDI class which we shall deal with in the following.

IV. BDI CLASS

A. \mathbb{Z} invariants

The Hamiltonian in the BDI class also satisfies the three intrinsic symmetries listed in Eq.(3), except that the time-reversal operator has the property $T^2 = 1$. This key difference determines that Fermi level crossings on high-symmetry lines in the parameter space do not necessarily come in pairs, due to the absence of Kramers degeneracy, as illustrated schematically in Fig. 8(b). However, time-reversal symmetry still ensures that a crossing off the high-symmetry lines, say at (k_F, λ_F) , has a partner at $(-k_F, \lambda_F)$, only the two may not have opposite topological charges, as the D matrix doesn't satisfy the relation $D_a(k, \lambda) = -D_a^T(-k, \lambda)$. Hence each crossing within the pair needs to be examined individually. Consequently, the higher-order topological invariants in this case are of \mathbb{Z} type.

In 2D, the BDI class does not have stable first-order topology but can exhibit nontrivial higher-order topology [2]. Here, we continue to consider systems with gapped bulk and edges, meaning that Hamiltonian $H_a(k, \lambda)$ is gapped for both $\lambda = 1$ and $\lambda = 0$. We may associate a topological invariant to the boundary-modulated Hamiltonian for generic λ , akin to the $\tilde{\nu}_a(\lambda)$ in Eq.(6) for the DIII class. The topological invariant in the BDI class is the winding number of D matrix along the loop with constant k and takes the form

$$\tilde{\omega}_a(\lambda) = \frac{1}{2\pi i} \int_{-\pi}^{\pi} dk \partial_k \ln \det[D_a(k, \lambda)]. \quad (30)$$

Similar to the DIII class, the higher-order topological invariant ω_a here is defined to be the first-order topological invariant of the quasi-1D cylindrical Hamiltonian $H_a(k, 0)$, i.e.,

$$\omega_a = \tilde{\omega}_a(0). \quad (31)$$

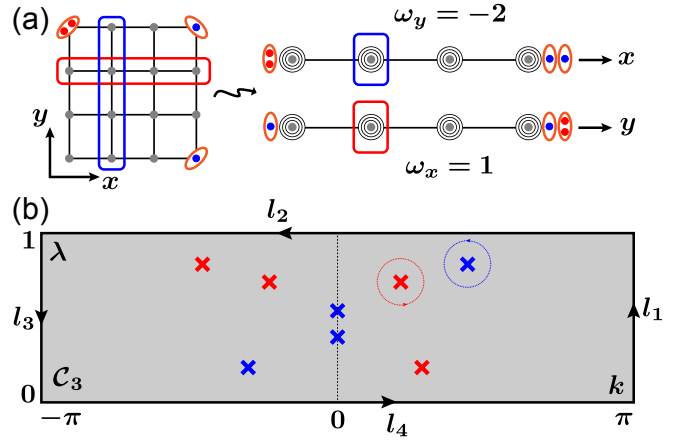


FIG. 8. (a) The relation between higher-order topological invariants and Majorana corner modes in the BDI class. The invariant ω_y corresponds to the difference in the number of Majorana zero modes with opposite chiralities at two corners on the left, while ω_x counts the two bottom corners. Blue and red dots represent Majorana modes with chiralities $+1$ and -1 , respectively. (b) Fermi level crossings in the BDI class. The crossings off high-symmetry lines always come in pairs. On the line, the crossing may appear alone. In contrast to the DIII class, signs of topological charges for time-reversal partners, as indicated by colors of the crosses, can be identical.

Meanwhile, $\tilde{\omega}_a(1)$ indicates the first-order topology of a toroidal system and is hence always zero.

Following from Eqs.(30) and (31), ω_a may take any integer value. In a 1D system, this invariant reflects the difference in the count of Majorana zero modes with distinct chiralities (± 1), namely the eigenvalues of chiral operator, at one end. For the Hamiltonian $H_a(k, \lambda)$ in consideration, we may denote $N_{a\pm}^{L(R)}$ as the number of Majorana zero modes at left (right) end with chirality ± 1 . Then we have

$$\omega_a = N_{a+}^L - N_{a-}^L = N_{a-}^R - N_{a+}^R. \quad (32)$$

In a truly 1D system, Majorana zero modes of different chiralities can couple, resulting in only one type of Majorana modes residing at each end if no other symmetries are enforced. However, in the quasi-1D system here, each end, comprising two spatially separated corners, can accommodate stable Majorana corner modes of different types, as depicted in Fig. 8(a). The system enters nontrivial higher-order phases when one or both of the invariants (ω_x, ω_y) take nonzero values.

To establish the relationship between higher-order invariants and Fermi level crossings, we consider a large loop, \mathcal{C}_3 , along the boundary of the parameter space. This loop consists of four line segments, l_1 to l_4 , as depicted in Fig. 8(b). The winding number of the D matrix

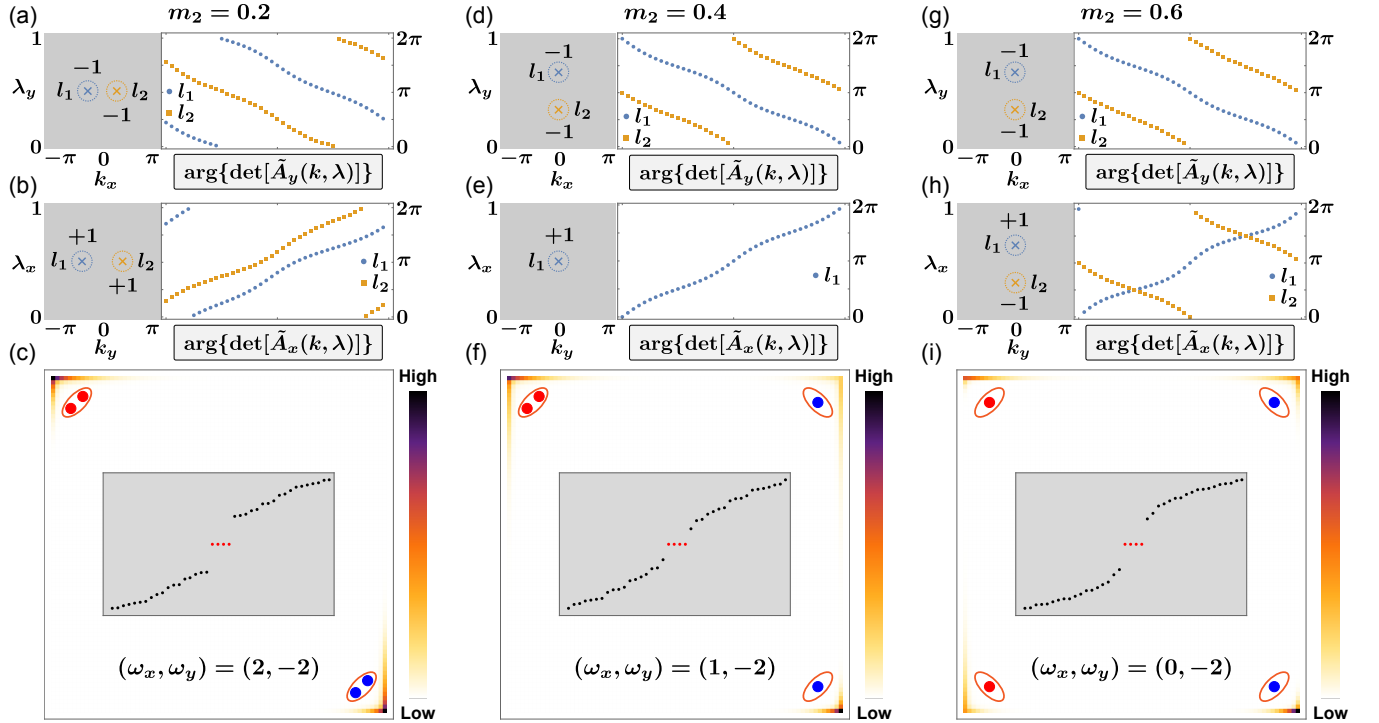


FIG. 9. Fermi level crossings and higher-order topological invariants in three distinct phases of the BDI model. The pair of higher-order invariants, (ω_x, ω_y) , is determined by topological charges of Fermi level crossings. In (a-b), (d)-(e) and (g)-(h), the crosses mark the relative positions of Fermi level crossings, and the numbers adjacent to each cross indicate their respective topological charges, which are obtained from winding numbers of the D matrix along loops, l_1 and l_2 , enclosing each crossing. (c), (f), (i) The distributions of Majorana corner modes. The solid blue and red circles represent Majorana zero modes with chiralities $+1$ and -1 , respectively. Insets showcase energy spectra for an 80×80 open-boundary system. In these plots, $m_1 = 0.3t$ and $\delta m = 0.1t$.

along this giant loop is given by

$$\begin{aligned} \Omega &= \frac{1}{2\pi i} \sum_{i=1}^4 \int_{l_i} dl \nabla_l \ln \det[D_a(k, \lambda)] \\ &= \sum_{(k_F, \lambda_F)} n_a(k_F, \lambda_F), \end{aligned} \quad (33)$$

where the summation in the last equality runs over all Fermi level crossings in the parameter space. The line integrals along l_1 and l_3 exactly cancel each other. We are thus left with integrals along l_2 and l_4 , which essentially represent the winding number $\tilde{\omega}(1)$ and $\tilde{\omega}(0)$ as defined in Eq.(30), up to a sign difference. Hence we have

$$\Omega = \tilde{\omega}_a(0) - \tilde{\omega}_a(1). \quad (34)$$

Given that $\tilde{\omega}_a(1) = 0$, we now arrive at the relation between higher-order topological invariants and Fermi level crossings, which reads

$$\omega_a = \sum_{(k_F, \lambda_F)} n_a(k_F, \lambda_F). \quad (35)$$

It follows from Eq.(35) that the sign of the topological charge for each crossing matters, and that all the Fermi level crossings together determine the overall higher-order topological invariants.

B. An example

As a demonstration, we consider a 2D Hamiltonian in the BDI class, which is based on the model described in Eq.(27). The Hamiltonian takes the form

$$H_{\text{BDI}}(\mathbf{k}) = H_{\text{DIII}}(\mathbf{k}) - m_2 \sigma_y. \quad (36)$$

Due to the additional σ_y term, this Hamiltonian does not preserve time-reversal symmetry of the DIII-class Hamiltonian, which is $T = -i\sigma_y \mathcal{K}$. Instead, the model exhibits a different time-reversal symmetry with $T = \sigma_x \mathcal{K}$. Since the latter time-reversal operator satisfies $T^2 = 1$, the Hamiltonian falls into BDI classification. The chiral symmetry operator is now represented as $S = \tau_x \sigma_x$.

In the case where $m_1 = m_2 = 0$, the system could possibly host a pair of Fermi level crossings on high-symmetry lines, depending on the relative strength of m and δm . We already know that m_1 term doesn't couple the two crossings but instead separates them and drives them away from the high-symmetry lines. The m_2 term doesn't couple them either, albeit for a different reason. Due to the redefined chiral symmetry, the two crossings within the pair now carry the same topological charge, implying they cannot annihilate with each other. At the onset of m_2 , the pair moves along the high-symmetry

line in opposite directions. In this situation, turning on m_1 cannot immediately move each crossing off the line because of the time-reversal symmetry. However, for sufficiently large m_1 , the two separated crossings may meet again. If we continue to increase m_1 , the pair would move off the line. Therefore, the positions of the two crossings vary according to the relative strength of m_1 and m_2 . When the m_1 term is dominant, one might anticipate that the pair of Fermi level crossings will occur off the high-symmetry lines at $(\pm k_F, \lambda_F)$. On the contrary, if the m_2 term is large compared to m_1 , they may both reside on the high-symmetry lines, but at distinct points.

To illustrate these arguments, we present three representative cases with varying m_2 in Fig. 9. It's evident that the number and positions of Fermi level crossings, along with their topological charges, differ in each case, leading to distinct topological invariants. For smaller m_2 , two crossings appear off the high-symmetry lines and have identical topological charges, as shown in Figs. 9(a)-(c). Following Eq.(35), we determine the topological invariants to be $(\omega_x, \omega_y) = (2, -2)$. As a result, four Majorana zero modes are found distributed across two opposite corners. At each corner, the two zero modes share the same chirality, as indicated by colors of the solid circles in Fig. 9(c). These topological invariants are further corroborated using Eq.(32), by noting that $N_{x-}^L = N_{y+}^L = 0$ and $N_{x+}^L = N_{y-}^L = 2$.

As m_2 increases, the two crossings are driven towards the high-symmetry line $K = 0$ where they will meet with each other. Subsequently, the pair is pushed in opposite directions along the line. One of the crossings gradually approaches $\lambda = 0$, and annihilate with its counterpart at negative λ . As depicted in Figs. 9(d) and (e) for $m = 0.4$, two crossings are located on the line $K = 0$ in the (k_x, λ_y) space, whereas only one crossing are left in the (k_y, λ_x) space as the other one has annihilated with the crossing with $-\lambda_x$ when they meet at $\lambda_x = 0$. In this case, the topological invariants are $(\omega_x, \omega_y) = (1, -2)$. There are still four Majorana zero modes at the corners, but their distribution varies from the previous case. As shown in Fig. 9(f), two Majorana zero modes with chirality -1 group in one corner, while the others with chirality $+1$ occupy two separate corners, i.e., $N_{x+}^L = 1$, $N_{x-}^L = N_{y+}^L = 0$ and $N_{y-}^L = 2$.

With a further increase in m_2 , the two crossings in the (k_x, λ_y) space remain. In the (k_y, λ_x) space, however, another crossing emerges on the high-symmetry line carrying an opposite charge. We then have $(\omega_x, \omega_y) = (0, -2)$. Four Majorana modes are still present, but their locations differ from the previous cases. Now, each corner hosts one Majorana mode, with $N_{x+}^L = 1$, $N_{x-}^L = 1$, $N_{y+}^L = 0$ and $N_{y-}^L = 2$.

In all three cases, at least one of the two invariants is nonzero, indicating the nontrivial higher-order topology. It is possible that two systems with identical topological invariants can have distinct distributions, or even different numbers of Majorana corner modes. Nonetheless, the presence of nontrivial higher-order topology in BDI class

is assured whenever at least one of the invariants assumes a nonzero value.

V. DISCUSSIONS AND CONCLUSIONS

We have established that Fermi level crossings can act as indicators for higher-order topology in DIII and BDI classes. With variations in a bulk parameter, topological phase transitions may occur when either the number or the topological charges of these crossings change, even if the bulk gap remains open. The close relationship between Fermi level crossings and the bulk Hamiltonian directly illustrates the bulk-boundary correspondence in higher-order topological superconductors, irrespective of crystalline symmetries. The fact that Fermi level crossings could change when either the bulk or edge gap closes, highlights a striking contrast to conventional bulk-boundary correspondence, where topological phase transitions typically occur only when the bulk gap closes.

In the DIII class, the \mathbb{Z}_2 charge for crossings on high-symmetry lines is obtained from the root's multiplicity by solving Eq.(24) in the case of linear band crossings. For other types of crossings, this argument still holds. Let's first consider a pair of band crossings at (K, λ_F) , which means only $m_{a,1}$ in Eq.(13) equals zero at the crossing, and assume $m_{a,1} \propto (\lambda - \lambda_F)^r$ near the crossing. The exponent r indicates the type of crossings. Apparently, only if r is odd will $m_{a,1}$ change its sign after crossing λ_F . Hence, $\eta_a = 1$ for odd r and $\eta_a = 0$ for even r . For instance, the quadratic band crossing corresponds to $r = 2$, in which case $\eta_a = 0$, suggesting that the Pfaffian of the D matrix doesn't experience a π -phase jump across λ_F . Given that $\det[D_a(K, \lambda)] \propto (\lambda - \lambda_F)^{2r}$ near the crossing, we immediately obtain the root's multiplicity as $p_a = 2r$. The parity of $p_a/2$ is exactly equal to that of η_a . For a generic case, η_a is given by the number of $m_{a,j}$ that changes sign after crossing λ_F , which equals the number of crossing pairs with odd r . The root's multiplicity is expressed as $p_a = 2\rho_r r$, where ρ_r represents the number of crossing pairs with exponent r . One can verify that $p_a/2 \bmod 2 = \eta_a \bmod 2$. Therefore, the \mathbb{Z}_2 charge of Fermi level crossings on the high-symmetry lines can be determined by the root's multiplicity, independent of the crossing type. For a crossing away from the high-symmetry lines, it is necessary to evaluate its topological charge defined in Eq.(26), which carries opposite charge to its time-reversal partner. In this case, the \mathbb{Z}_2 charge defined for the time-reversal pair is nonzero when the topological charge of either crossing within the pair is odd. An interesting question arises about whether one may determine the \mathbb{Z}_2 charge based solely on the root's multiplicity, akin to the crossings on high-symmetry lines. For example, consider two crossings off high-symmetry lines at $(\pm k_F, \lambda_F)$, each with multiplicity p_a . If we move these crossings towards the high-symmetry lines, which doesn't affect the \mathbb{Z}_2 charge, the multiplicity at the meeting point (K, λ_F)

on the high-symmetry lines becomes $2p_a$ unless the crossing type changes in this process. This implies that under these conditions, the \mathbb{Z}_2 charge could be inferred from the root's multiplicity. However, it's challenging to conclusively prove that the crossing type remains the same, which means we don't know whether p_a remains constant before the crossing pair arrive at the high-symmetry lines, though it seems unlikely to change in most cases. In the model we studied in Sec. IIID, p_a for crossings off the high-symmetry lines doesn't change while the crossings move. In BDI classes, the distinction between Fermi level crossings on and off high-symmetry lines becomes irrelevant, and the root's multiplicity seems also to lose its significance. Here, the higher-order invariants rely on the cumulative topological charges of all crossings.

In this paper, we've characterized higher-order topology through pairs of topological invariants: (ν_x, ν_y) for the DIII class, as defined in Eq.(15), and (ω_x, ω_y) for the BDI class, introduced in Eq.(35). A system enters nontrivial higher-order phases when at least one of these invariants becomes nonzero. However, the reverse isn't necessarily true. Nontrivial higher-order topology can occur even if both topological invariants are zero. For example, in the DIII class, if Majorana Kramers pairs are present at all four corners, the invariants may still be zero, $(\nu_x, \nu_y) = 0$. This happens because these invariants represent the first-order topology of a quasi-1D cylindrical system, where each end corresponds to two corners in a square sample. When each corner supports a Majorana pair in the DIII class, their combined effect results in trivial invariants, due to the \mathbb{Z}_2 classification. A similar scenario occurs in the BDI class, where trivial invariants can arise if the two corners at each end host Majorana zero modes with opposing chiralities. This can also be viewed from the perspective of edge topology, where these invariants actually indicate the topological differences between opposite edges, as we have established in our previous study of D-class systems [46]. However, in higher-order topological phases, topological differences may only exist between adjacent edges, rendering these invariants inadequate. For a comprehensive bulk-boundary correspondence in such cases, other general twisted boundary conditions, involving phase modulations of the boundary Hamiltonian, might be necessary [37, 52–56]. Our research underscores that boundary condition modulation can reveal a direct connection between bulk and corners. Future explorations within this framework may encompass a wider array of higher-order phases.

In summary, our study delves into 2D higher-order topological superconductors in the DIII and BDI classes, both characterized by the presence of chiral symmetry. We demonstrate that Fermi level crossings, occurring when boundary conditions vary, can act as reliable indicators of nontrivial higher-order topology. These crossings also provide a direct and intuitive understanding of how bulk properties influence the emergence of Majorana zero modes at the corners. A pair of higher-order topological invariants are introduced, which are associated

with topological charges of Fermi level crossings. The invariants indicate nontrivial higher-order phases when at least one of them assumes a nonzero value.

ACKNOWLEDGMENTS

This work was supported by National Science Foundation of China (NSFC) under Grant No. 11704305, and the Innovation Program for Quantum Science and Technology (2021ZD0302400).

Appendix A: The matrix \tilde{A}_a

In this appendix, we will present the details in deriving the matrix $\tilde{A}_a(k, \lambda)$ introduced in Eq.(23), whose determinant is shown to be equal to that of $A_a(k, \lambda)$ in Eq.(21).

Firstly, we note that the D matrix of bulk Hamiltonian in momentum space is given by $D(\mathbf{k}) = u^\dagger H(\mathbf{k})v$, where $U_S = (u \ v)$ is the unitary matrix that diagonalizes the chiral symmetry operator S . For the boundary-modulated Hamiltonian $H_a(k, \lambda)$ represented in the basis $\Psi_a(k) = \{\psi_{a,1}(k), \dots, \psi_{a,j}(k), \dots, \psi_{a,N_a}(k)\}$, with $\psi_{a,j}(k)$ including all internal degrees of freedom, denoted as $[c_a(k)]_{j\alpha}$, on the site j , the corresponding matrices u and v are replaced by $u_a = \mathbb{1}_{N_a \times N_a} \otimes u$ and $v_a = \mathbb{1}_{N_a \times N_a} \otimes v$, respectively. Here, N_a represents the number of unit cells along the a direction. As such, the D matrix of boundary-modulated Hamiltonian is given by $D_a(k, \lambda) = u_a^\dagger H_a(k, \lambda)v_a$, and similarly for the boundary Hamiltonian $D_a^b(k) = u_a^\dagger B_a(k)v_a$. The entries of A_a can be written as

$$[A_a(k, \lambda)]_{i\bar{\alpha}, j\bar{\beta}} = \delta_{ij} \delta_{\bar{\alpha}\bar{\beta}} - (1 - \lambda) \times [D_a^{-1}(k, 1)]_{i\bar{\alpha}, l\bar{\gamma}} [D_a^b(k)]_{l\bar{\gamma}, j\bar{\beta}}, \quad (\text{A1})$$

with Einstein summation assumed. In Eq.(A1) we distinguish $\bar{\alpha}$ and $\bar{\beta}$ from α and β as the former indices run over only half the inner degrees of freedom. The two representations of bulk Hamiltonian, $D_a(k_{\bar{a}}, 1)$ and $D(\mathbf{k})$, are related with each other through Fourier transformation, represented in matrix form as

$$[D_a(k_{\bar{a}}, 1)]_{i\bar{\alpha}, j\bar{\beta}} = \sum_{k_a} [U_F^\dagger]_{i, k_a} [D(\mathbf{k})]_{\bar{\alpha}, \bar{\beta}} [U_F]_{k_a, j}. \quad (\text{A2})$$

Here, the subscript of k is explicitly shown for clarity, and the Fourier matrix $[U_F]_{k_a, j} = \frac{1}{\sqrt{N_a}} e^{-ij k_a}$. Since the boundary Hamiltonian operates only on boundary cells, it follows that the entries $[A_a(k, \lambda)]_{i\bar{\alpha}, j\bar{\beta}} = \delta_{ij} \delta_{\bar{\alpha}\bar{\beta}}$ if j does not represent a boundary cell. Consequently, the determinant of A_a can be calculated using only the block corresponding to boundary cells, denoted by $\bar{A}_a(k, \lambda)$, with

$$\det[A_a(k, \lambda)] = \det[\bar{A}_a(k, \lambda)]. \quad (\text{A3})$$

Combing Eqs.(A1) and (A2), we arrive at

$$[\bar{A}_a(k_{\bar{a}}, \lambda_a)]_{i_b, \bar{\alpha}, j_b, \bar{\beta}} = \delta_{i_b, j_b} \delta_{\bar{\alpha}, \bar{\beta}} - \frac{1}{2\pi}(1 - \lambda_a) \quad (\text{A4})$$

$$\times \int dk_a [F(k_a)]_{i_b, l_b} [D^{-1}(\mathbf{k})]_{\bar{\alpha}, \bar{\gamma}} [\bar{D}_a^b(k_{\bar{a}})]_{l_b, \bar{\gamma}, j_b, \bar{\beta}},$$

where \bar{D}_a^b represents the block of D_a^b corresponding to boundary cells labelled by i_b, j_b , $[F(k_a)]_{i_b, l_b} = e^{ik_a(i_b - l_b)}$, and the summation over k_a is replaced by integration.

In certain cases, $\bar{D}_a^b(k)$ may not be a full-rank matrix. Its singular value decomposition is represented as

$$[\bar{D}_a^b(k)]_{i_b, \bar{\alpha}, j_b, \bar{\beta}} = [\bar{U}_a^b(k)]_{i_b, \bar{\alpha}, n} [\bar{\Lambda}_a^b(k)]_{n, n} [\bar{V}_a^{b\dagger}(k)]_{n, j_b, \bar{\beta}}, \quad (\text{A5})$$

where $\bar{\Lambda}_a^b$ is a diagonal matrix with r_a nonzero entries, with r_a representing the rank of $\bar{D}_a^b(k)$. In addition, $\bar{\Lambda}_a^b$ can be arranged such that $[\bar{\Lambda}_a^b]_{n, n} \neq 0$ for $n \leq r_a$. Given that \bar{U}_a^b and \bar{V}_a^b are unitary matrices, it follows that

$$\det[\bar{A}_a(k, \lambda)] = \det[\bar{V}_a^{b\dagger}(k) \bar{A}_a(k, \lambda) \bar{V}_a^b(k)]. \quad (\text{A6})$$

From Eqs.(A4) and (A5) we know $[\bar{V}_a^{b\dagger} \bar{A}_a \bar{V}_a^b]_{m, n} = \delta_{m, n}$ if $n > r_a$. Hence we only need to consider the entries where $m, n \leq r_a$ while calculating its determinant. For convenience, we group the first r_a columns of \bar{V}_a^b into a new matrix, denoted as \tilde{V}_a^b . Define

$$\tilde{A}_a(k, \lambda) = \tilde{V}_a^{b\dagger}(k) \bar{A}_a(k, \lambda) \tilde{V}_a^b(k), \quad (\text{A7})$$

and thus

$$\det[\bar{A}_a(k, \lambda)] = \det[\tilde{A}_a(k, \lambda)]. \quad (\text{A8})$$

Combining Eqs.(A4) and (A7) we arrive at Eq.(23) in the main text, which shows the specific form of this $r_a \times r_a$ matrix $\tilde{A}_a(k, \lambda)$.

-
- [1] X.-L. Qi and S.-C. Zhang, Topological insulators and superconductors, *Rev. Mod. Phys.* **83**, 1057 (2011).
- [2] C.-K. Chiu, J. C. Y. Teo, A. P. Schnyder, and S. Ryu, Classification of topological quantum matter with symmetries, *Rev. Mod. Phys.* **88**, 035005 (2016).
- [3] N. Read and D. Green, Paired states of fermions in two dimensions with breaking of parity and time-reversal symmetries and the fractional quantum Hall effect, *Phys. Rev. B* **61**, 10267 (2000).
- [4] A. Y. Kitaev, Unpaired Majorana fermions in quantum wires, *Phys.-Usp.* **44**, 131 (2001).
- [5] F. Wilczek, Majorana returns, *Nature Phys* **5**, 614 (2009).
- [6] J. Alicea, New directions in the pursuit of Majorana fermions in solid state systems, *Rep. Prog. Phys.* **75**, 076501 (2012).
- [7] T. D. Stanescu and S. Tewari, Majorana fermions in semiconductor nanowires: Fundamentals, modeling, and experiment, *J. Phys.: Condens. Matter* **25**, 233201 (2013).
- [8] C. Beenakker, Search for Majorana Fermions in Superconductors, *Annu. Rev. Condens. Matter Phys.* **4**, 113 (2013).
- [9] S. R. Elliott and M. Franz, *Colloquium* : Majorana fermions in nuclear, particle, and solid-state physics, *Rev. Mod. Phys.* **87**, 137 (2015).
- [10] R. Aguado, Majorana quasiparticles in condensed matter, *Riv. Nuovo Cimento* **40**, 523 (2017).
- [11] W. A. Benalcazar, B. A. Bernevig, and T. L. Hughes, Quantized electric multipole insulators, *Science* **357**, 61 (2017).
- [12] W. A. Benalcazar, B. A. Bernevig, and T. L. Hughes, Electric multipole moments, topological multipole moment pumping, and chiral hinge states in crystalline insulators, *Phys. Rev. B* **96**, 245115 (2017).
- [13] J. Langbehn, Y. Peng, L. Trifunovic, F. von Oppen, and P. W. Brouwer, Reflection-Symmetric Second-Order Topological Insulators and Superconductors, *Phys. Rev. Lett.* **119**, 246401 (2017).
- [14] Z. Song, Z. Fang, and C. Fang, (d - 2) -Dimensional Edge States of Rotation Symmetry Protected Topological States, *Phys. Rev. Lett.* **119**, 246402 (2017).
- [15] F. Schindler, A. M. Cook, M. G. Vergniory, Z. Wang, S. S. P. Parkin, B. A. Bernevig, and T. Neupert, Higher-order topological insulators, *Sci. Adv.* **4**, eaat0346 (2018).
- [16] F. Schindler, Z. Wang, M. G. Vergniory, A. M. Cook, A. Murani, S. Sengupta, A. Y. Kasumov, R. Deblock, S. Jeon, I. Drozdov, H. Bouchiat, S. Guéron, A. Yazdani, B. A. Bernevig, and T. Neupert, Higher-order topology in bismuth, *Nature Phys* **14**, 918 (2018).
- [17] W. A. Benalcazar and A. Cerjan, Chiral-Symmetric Higher-Order Topological Phases of Matter, *Phys. Rev. Lett.* **128**, 127601 (2022).
- [18] E. Khalaf, Higher-order topological insulators and superconductors protected by inversion symmetry, *Phys. Rev. B* **97**, 205136 (2018).
- [19] X. Zhu, Tunable Majorana corner states in a two-dimensional second-order topological superconductor induced by magnetic fields, *Phys. Rev. B* **97**, 205134 (2018).
- [20] Z. Yan, F. Song, and Z. Wang, Majorana Corner Modes in a High-Temperature Platform, *Phys. Rev. Lett.* **121**, 096803 (2018).
- [21] Q. Wang, C.-C. Liu, Y.-M. Lu, and F. Zhang, High-Temperature Majorana Corner States, *Phys. Rev. Lett.* **121**, 186801 (2018).
- [22] Y. Wang, M. Lin, and T. L. Hughes, Weak-pairing higher order topological superconductors, *Phys. Rev. B* **98**, 165144 (2018).
- [23] Z. Yan, Higher-Order Topological Odd-Parity Superconductors, *Phys. Rev. Lett.* **123**, 177001 (2019).
- [24] R.-X. Zhang, W. S. Cole, and S. Das Sarma, Helical Hinge Majorana Modes in Iron-Based Superconductors, *Phys. Rev. Lett.* **122**, 187001 (2019).
- [25] A. K. Ghosh, T. Nag, and A. Saha, Hierarchy of higher-

- order topological superconductors in three dimensions, *Phys. Rev. B* **104**, 134508 (2021).
- [26] H. D. Scammell, J. Ingham, M. Geier, and T. Li, Intrinsic first- and higher-order topological superconductivity in a doped topological insulator, *Phys. Rev. B* **105**, 195149 (2022).
- [27] M. Geier, L. Trifunovic, M. Hoskam, and P. W. Brouwer, Second-order topological insulators and superconductors with an order-two crystalline symmetry, *Phys. Rev. B* **97**, 205135 (2018).
- [28] L. Trifunovic and P. W. Brouwer, Higher-Order Bulk-Boundary Correspondence for Topological Crystalline Phases, *Phys. Rev. X* **9**, 011012 (2019).
- [29] A. Skurativska, T. Neupert, and M. H. Fischer, Atomic limit and inversion-symmetry indicators for topological superconductors, *Phys. Rev. Research* **2**, 013064 (2020).
- [30] S. Ono, H. C. Po, and H. Watanabe, Refined symmetry indicators for topological superconductors in all space groups, *Sci. Adv.* **6**, eaaz8367 (2020).
- [31] R. Takahashi, Y. Tanaka, and S. Murakami, Bulk-edge and bulk-hinge correspondence in inversion-symmetric insulators, *Phys. Rev. Research* **2**, 013300 (2020).
- [32] Y.-T. Hsu, W. S. Cole, R.-X. Zhang, and J. D. Sau, Inversion-protected Higher-order Topological Superconductivity in Monolayer WTe₂, *Phys. Rev. Lett.* **125**, 097001 (2020).
- [33] J. Kruthoff, J. de Boer, J. van Wezel, C. L. Kane, and R.-J. Slager, Topological Classification of Crystalline Insulators through Band Structure Combinatorics, *Phys. Rev. X* **7**, 041069 (2017).
- [34] F. Tang, H. C. Po, A. Vishwanath, and X. Wan, Comprehensive search for topological materials using symmetry indicators, *Nature* **566**, 486 (2019).
- [35] T. Zhang, Y. Jiang, Z. Song, H. Huang, Y. He, Z. Fang, H. Weng, and C. Fang, Catalogue of topological electronic materials, *Nature* **566**, 475 (2019).
- [36] M. G. Vergniory, L. Elcoro, C. Felser, N. Regnault, B. A. Bernevig, and Z. Wang, A complete catalogue of high-quality topological materials, *Nature* **566**, 480 (2019).
- [37] R.-X. Zhang, Bulk-Vortex Correspondence of Higher-Order Topological Superconductors (2022), arxiv:2208.01652.
- [38] E. Roberts, J. Behrends, and B. Béri, Second-order bulk-boundary correspondence in rotationally symmetric topological superconductors from stacked Dirac Hamiltonians, *Phys. Rev. B* **101**, 155133 (2020).
- [39] S.-J. Huang and Y.-T. Hsu, Faithful derivation of symmetry indicators: A case study for topological superconductors with time-reversal and inversion symmetries, *Phys. Rev. Research* **3**, 013243 (2021).
- [40] F. Tang, S. Ono, X. Wan, and H. Watanabe, High-Throughput Investigations of Topological and Nodal Superconductors, *Phys. Rev. Lett.* **129**, 027001 (2022).
- [41] X. Zhu, Second-Order Topological Superconductors with Mixed Pairing, *Phys. Rev. Lett.* **122**, 236401 (2019).
- [42] E. Khalaf, W. A. Benalcazar, T. L. Hughes, and R. Queiroz, Boundary-obstructed topological phases, *Phys. Rev. Research* **3**, 013239 (2021).
- [43] A. Tiwari, A. Jahin, and Y. Wang, Chiral Dirac superconductors: Second-order and boundary-obstructed topology, *Phys. Rev. Research* **2**, 043300 (2020).
- [44] Y. Volpez, D. Loss, and J. Klinovaja, Second-Order Topological Superconductivity in π -Junction Rashba Layers, *Phys. Rev. Lett.* **122**, 126402 (2019).
- [45] X. Wu, W. A. Benalcazar, Y. Li, R. Thomale, C.-X. Liu, and J. Hu, Boundary-Obstructed Topological High- T_c Superconductivity in Iron Pnictides, *Phys. Rev. X* **10**, 041014 (2020).
- [46] H. Wang and X. Zhu, Higher-order topological superconductors characterized by Fermi level crossings, *Phys. Rev. B* **108**, 125426 (2023).
- [47] Y. Tanaka, R. Takahashi, and S. Murakami, Appearance of hinge states in second-order topological insulators via the cutting procedure, *Phys. Rev. B* **101**, 115120 (2020).
- [48] A. P. Schnyder and S. Ryu, Topological phases and surface flat bands in superconductors without inversion symmetry, *Phys. Rev. B* **84**, 060504(R) (2011).
- [49] X.-L. Qi, T. L. Hughes, and S.-C. Zhang, Topological invariants for the Fermi surface of a time-reversal-invariant superconductor, *Phys. Rev. B* **81**, 134508 (2010).
- [50] J.-W. Rhim, J. H. Bardarson, and R.-J. Slager, Unified bulk-boundary correspondence for band insulators, *Phys. Rev. B* **97**, 115143 (2018).
- [51] M. Wimmer, Algorithm 923: Efficient Numerical Computation of the Pfaffian for Dense and Banded Skew-Symmetric Matrices, *ACM Trans. Math. Softw.* **38**, 1 (2012).
- [52] Q. Niu, D. J. Thouless, and Y.-S. Wu, Quantized Hall conductance as a topological invariant, *Phys. Rev. B* **31**, 3372 (1985).
- [53] X.-L. Qi, Y.-S. Wu, and S.-C. Zhang, General theorem relating the bulk topological number to edge states in two-dimensional insulators, *Phys. Rev. B* **74**, 045125 (2006).
- [54] Z.-D. Song, L. Elcoro, and B. A. Bernevig, Twisted bulk-boundary correspondence of fragile topology, *Science* **367**, 794 (2020).
- [55] A. Jahin, Y.-M. Lu, and Y. Wang, Many-body higher-order topological invariant for C_n -symmetric insulators (2024), arxiv:2401.00050.
- [56] L. Lin and C. Lee, Probing Chiral-Symmetric Higher-Order Topological Insulators with Multipole Winding Number (2024), arxiv:2401.03699.